Spatiotemporal Wavelet Transform and the Multiscale Behavior of the Madden–Julian Oscillation*

KAZUYOSHI KIKUCHI AND BIN WANG

International Pacific Research Center, University of Hawaii at Manoa, Honolulu, Hawaii

ABSTRACT

Meteorological and geophysical phenomena involve multiple-scale processes. Here the spatiotemporal wavelet transform (STWT) is applied to detect significant, nonstationary, wave propagation signals from a time–space domain. One of the major advantages of the STWT is the capability to localize the wave properties in both space and time, which facilitates the study of interactions among multiple-scale disturbances by providing relevant information about energy concentration at a given time and space. The global wavelet spectrum (*scalogram*) of the STWT, which gives an integrated view of the spectrum as wavenumber and frequency, provides a lucid picture of the spectral power distribution that is consistent with the result obtained from the Fourier-based space–time power spectrum. The STWT has also the capability of reconstruction and thus can be used as a spatiotemporal wave filter.

The STWT analysis is applied to analyze the multiscale structure of the Madden–Julian oscillation (MJO) studied by Nakazawa. All types of convectively coupled equatorial waves were identified. The analysis results reveal the structural differences between the MJO and Kelvin waves and their different relationships with the embedded westward propagating inertio-gravity (WIG) waves: for the Kelvin wave the enhanced activity of the WIG waves coincides with the most active convective area, whereas for the MJO the enhanced WIG waves occur to the east of the MJO convective center. In addition, the WIG waves in the MJO have shorter wavelengths and periods, but those in the Kelvin waves have longer wavelengths and periods. This difference may hold a key to understanding the propagation speed difference between the MJO and Kelvin waves. The possible "upscale feedback" of the WIG waves on the MJO and Kelvin waves is also discussed.

1. Introduction

Atmospheric and oceanic motions occur on a variety of temporal and spatial scales. These motions with different scales are normally interactive rather than independent of each other. Multiscale interaction is thus an essential process in atmospheric and oceanic sciences. However, the complex nature of the multiscale interaction remains a major challenge for designing an effective method to analyze it.

Wavelet transform (WT) is one of the tools for analysis of the multi-time-scale behavior in general in time domain.

The WT was originally invented to investigate nonstationary processes in the field of seismology (Morlet et al. 1982a,b) and has been used in a wide variety of fields including applied mathematics (e.g., Daubechies 1992), signal processing (e.g., Addison 2002), and meteorology and geophysics (e.g., Meyers et al. 1993; Weng and Lau 1994; Lau and Weng 1995; Wang and Wang 1996). A comprehensive review of geophysical applications was given by Kumar and Foufoula-Georgiou (1997). A major function of the WT is to reveal the time–frequency localization of a signal, which enables one to depict how a given component at a given temporal scale varies with time.

One of the objectives of the present study is to introduce into the field of geophysics, especially atmospheric science, a wavelet analysis in both time and space [(1 + 1)-dimensional] domains, called spatiotemporal wavelet transform (STWT), or (1 + 1)-dimensional WT. Most previous WT analyses in geophysics utilized one-dimensional (1D) WT in the time domain and the STWT is virtually unknown. The STWT technique was

---

Corresponding author address: Kazuyoshi Kikuchi, International Pacific Research Center, University of Hawaii at Manoa, 1680 East–West Road, POST Bldg. 401, Honolulu, HI 96822.
E-mail: kazuyosh@hawaii.edu

originally designed to extract wave motion information from moving objects (e.g., Antoine et al. 2004). In this study we will show that the STWT can describe time–space variation of a given signal and thereby provide a powerful tool to document the multiscale behavior of a signal.

Another objective of this study is to apply the STWT to the equatorial convection and to examine multiscale structure and behavior of the Madden–Julian oscillation (MJO) (Madden and Julian 1971, 1972). The MJO is one of the most prominent phenomena in tropical and climate dynamics. Although the MJO is an equatorial trapped disturbance, it has huge impacts on other phenomena such as the Asian summer monsoon (e.g., Yasunari 1979; Sikka and Gadgil 1980), tropical cyclone formation and rapid intensification (e.g., Bessafi and Wheeler 2006; Frank and Roundy 2006; Wang and Zhou 2008), and tropical–extratropical interaction (e.g., Nitta 1987; Kawamura et al. 1996; Ding and Wang 2007). As shown by Nakazawa (1988), the MJO itself has a clear multiscale structure. In his conceptual model, a MJO that moves slowly eastward comprises several super cloud clusters (SCCs) moving eastward at faster speeds (10–15 m s^{-1}), with each SCC comprising a number of cloud clusters moving westward. The SCC has been identified as essentially the moist (convectively coupled) Kelvin waves (e.g., Takayabu and Murakami 1991), while westward propagating clusters were considered as inertio-gravity waves (e.g., Takayabu et al. 1996). In observations and theories, the structure and slow propagation of the MJO differs from the moist Kelvin waves (e.g., Wang 1988; Rui and Wang 1990; Wang and Rui 1990; Hendon and Salby 1994; Wheeler and Kiladis 1999). Due to the vanishing Coriolis force at the equator, the atmospheric and oceanic waves propagate in zonal directions (Matsuno 1966), providing an excellent case for examining signals in a time–longitude section along the equator with the use of the STWT.

Given the multiscale behavior of the MJO, it has been speculated that understanding of the multiscale interaction is a key to advance our understanding of the MJO dynamics (e.g., Majda and Biello 2004; Wang 2005; Moncrieff et al. 2007; Miura et al. 2007). The large-scale MJO may modulate the amplitude and change the properties (e.g., frequency, structure, and wavelength) of the small-scale component. The small-scale component, in turn, could feed back to the MJO by transporting heat, momentum, and moisture (e.g., Houze 2004; Moncrieff et al. 2007) and consequently modulate the amplitude and the properties of the MJO. Recent observational and theoretical studies have made significant progress in documentation and understanding of the MJO dynamics in terms of scale interaction. Straub and Kiladis (2003a) studied the relationship between the phase of

MJO and the activity of the Kelvin waves using 22-yr outgoing longwave radiation (OLR) data during boreal summer. Roundy (2008) examined the behavior of Kelvin waves with reference to the phase of the MJO. With a theoretical model, the interaction between the large-scale component and the embedded small scales has been demonstrated to play a critical role in understanding behavior of the MJO (Majda and Biello 2004; Majda et al. 2007). Despite this progress, study of the nonlinear *interaction* among convectively coupled equatorial waves remains a great challenge.

This paper consists of two parts. The first part (sections 2 through 4) is devoted to introducing the STWT to the field of geophysics, including the mathematical description of the theoretical development (section 2) and applied aspects (section 3) of the STWT, as well as demonstration of its application with an ideal example (section 4). Those readers who are primarily interested in the methodology may focus on these three sections. In the second part of the paper (sections 5 through 8) the STWT is applied to study the multiscale structures of the Nakazawa MJO case (section 5), the differences and relationships between the MJO and moist Kelvin waves (section 6), the modulation of the westward propagating inertio-gravity (WIG) waves by the MJO and Kelvin waves (section 7), and the possible feedback of the WIG waves onto the MJO and Kelvin waves (section 8). A summary is presented in the last section.

2. The spatiotemporal wavelet transform

Since the spatiotemporal wavelet transform (STWT) is unfamiliar to most people in the field of geophysics, we briefly document the STWT and define some useful parameters in this section. The concept of the method is of course not novel, but this section provides a mathematical basis for the STWT so that one can fully understand how it is derived and on what it is based.

a. Definition

The STWT can be obtained by extending the 1D WT by introducing a speed tuning parameter c as follows (e.g., Bouyoucef and Murenzi 1995):

$$W(b, \tau; a, c) = \int_{-\infty}^{\infty} dx \int_{-\infty}^{\infty} dt f(x, t)\psi_{b,\tau;a,c}^*(x, t), \quad (1)$$

where $W(b, \tau; a, c)$ is STWT, (x, t) the space–time position, $f(x, t)$ a space–time signal (real in most practical applications, but can be complex in the following discussion), and $\psi_{b,\tau;a,c}^*$ the analyzing wavelet with a spatiotemporal scale parameter $a > 0$ and a translation parameter $(b, \tau) \in \mathbf{R}^2$; $\psi_{b,\tau;a,c}^*$ designates the complex conjugate of $\psi_{b,\tau;a,c}$. It is clear that the STWT retains the

basic concept of WT; that is, the WT is defined by the inner products of a signal f with the wavelet. The analyzing wavelet in STWT can be expressed by means of a mother wavelet ψ as

$$\psi_{b,\tau;a,c}^*(x, t) = \frac{1}{a}\psi^*\left(\frac{x - b}{ac^{1/2}}, \frac{t - \tau}{ac^{-1/2}}\right). \qquad (2)$$

$$W(b, \tau; a, c) = a \int_{-\infty}^{\infty} dk \int_{-\infty}^{\infty} d\omega \hat{f}(k, \omega)\hat{\psi}^*(ac^{1/2}k, ac^{-1/2}\omega)e^{i(kb+\omega\tau)}, \qquad (3)$$

where the caret represents the Fourier transform and k and ω are respectively zonal wavenumber and temporal frequency.

b. Reconstruction and spatiotemporal filtering

Supposing we employ the continuous WT, the original signal can be reconstructed by means of the "*resolution of the identity*" formula (proof can be found in appendix A) as

$$f(x, t) = \frac{1}{C_\delta} \int_0^{\infty} \frac{da}{a^2} \int_0^{\infty} \frac{dc}{c} W(x, t; a, c), \qquad (4)$$

as long as the admissibility condition (A5) holds. This reconstruction formula can be used not only to check the program but also as a filter to extract a specific component of interest. The filtered field f' can be expressed as

$$f'(x, t) = \frac{1}{C_\delta} \iint_D \frac{da\, dc}{a^2\, c} W(x, t; a, c), \qquad (5)$$

where f' is constructed over a subset D of the domain: $D = \{(a, c) \in \mathbf{R}^2\}$. In practical applications, however, sometimes it would be more useful to define the integration domain $T \subset \{(k, \omega) \in \mathbf{R}^2\}$ in the corresponding Fourier zonal wavenumber–frequency space first. Then the domain D can be identified from the domain as $D = (a_M, c_M)(T)$, with the aid of a relationship between wavelet scales and Fourier wavelengths. Finally, f' can be obtained by the use of (5). For instance, in the case of

As in the 1D counterpart, the basic properties of the wavelet such as dilation and displacement are determined by a and (b, τ). In addition, c gives a phase speed in a Hovmöller diagram. In practical application, the STWT is computed in the Fourier space instead of physical space (1) as

the spatiotemporal Morlet function to be introduced later, the relationship between wavelet scales and Fourier wavelengths is given by (C4) and (C5). We shall follow this procedure as a spatiotemporal filter in section 4.

c. Energy conservation and wavelet scalograms (spectra)

One of the most important features of the WT is energy conservation. As in the 1D counterpart, conservation of total energy is retained in the STWT. The conservation of energy can be easily obtained as follows (proof can be found in appendix B):

$$\frac{1}{C_\psi} \int_0^{\infty} \frac{da}{a^3} \int_0^{\infty} \frac{dc}{c} \int_{-\infty}^{\infty} db \int_{-\infty}^{\infty} d\tau \left|W(b, \tau; a, c)\right|^2$$
$$= \int_{-\infty}^{\infty} dx \int_{-\infty}^{\infty} dt \left|f(x, t)\right|^2, \qquad (6)$$

where C_ψ is also a constant parameter depending only on ψ (B3). We can define the *wavelet energy density function* (also known as the *scalogram*), which represents the contribution to the signal energy at a given location (b, τ), scale a, and speed c as

$$P_w(b, \tau; a, c) = \left|W(b, \tau; a, c)\right|^2. \qquad (7)$$

Therefore, the relative contribution to the total energy by the given component defined by the domain D becomes

$$E' = \iint_D \frac{da\, dc}{a^3\, c} \int_{-\infty}^{\infty} db \int_{-\infty}^{\infty} d\tau P_w(b, \tau; a, c) \bigg/ \int_{-\infty}^{\infty} dx \int_{-\infty}^{\infty} dt \left|f(x, t)\right|^2. \qquad (8)$$

Also we can define the *global wavelet scalogram* to represent the global spectrum feature of the STWT as an average scalogram as follows:

$$\overline{P}_w(a, c) = \int_{b_1}^{b_2} db \int_{\tau_1}^{\tau_2} d\tau P_w(b, \tau; a, c). \qquad (9)$$

Similarly, we can define the *local wavelet scalogram*, which is designed to represent the energy of a given component at a given location (b, τ). Temporal and/or horizontal variations of the local wavelet scalogram thus depict how a given component varies with time and/or space—in other words, how a given component is

modulated by another component if careful examination is made. Considering the conservation of energy, the local wavelet scalogram in given ranges of scale and phase speed can be written as

$$\overline{P}_w(b, \tau) = \frac{1}{C_\psi} \iint_D \frac{dc}{c} \frac{da}{a^3} P_w(b, \tau; a, c). \quad (10)$$

d. Selection of the STWT mother function

In this study, we chose the spatiotemporal Morlet function, one of the most popular selections, as the directional mother function:

$$\psi(x, t) = e^{i(k_0' x + \omega_0' t)} e^{-1/2(x^2 + t^2)}; \quad (11)$$

consequently in the Fourier space

$$\hat{\psi}(k, \omega) = \hat{\psi}^*(k, \omega) = e^{-1/2(k - k_0')^2} e^{-1/2(\omega - \omega_0')^2}, \quad (12)$$

where $|k_0'| = 6$ and $\omega_0' = 6$ to ensure the admissibility condition since the equivalent condition $\hat{\psi}^*(\mathbf{0}) = \mathbf{0}$ approximately holds in this case. Since $\omega_0' > 0$, only positive ω_0' values are analyzed, and positive or negative k_0' parameters are used to analyze positive or negative k values, that is, westward or eastward propagating patterns, respectively. Note that the results to be shown later are not sensitive to the selection of a different reasonable directional mother function. Moreover, selecting the ST Morlet function as a mother function is a reasonable extension of the Fourier analysis to localize a signal because the ST Morlet wavelet has a plane wave form in both space and time localized with a Gaussian envelope in both directions. The analyzing wavelet (2) therefore is able to express a localized signal that has a wave form characterized by different spatiotemporal scales and phase speeds.

3. Application issues

a. Consideration of statistical significance level in STWT

Here we consider how to assess the statistical significance level in STWT, which is an important aspect to identify significant signals. Since we focus on the introduction and application of STWT in the field of atmospheric science, we avoid complex and complete derivation based on a theoretical framework. Instead, we try to develop a reasonable framework based on the previous findings, but the essence of the framework is correct.

Torrence and Compo (1998) developed a method to assess the statistical significance level in the 1D WT on the basis of Monte Carlo simulations. They showed that the local wavelet power spectrum $|W(a, b)|^2/\sigma^2$ has a χ_2^2 distribution

$$\frac{|W(b; a)|^2}{\sigma^2} \Rightarrow \frac{1}{2} P_k \chi_2^2, \quad (13)$$

where σ^2 is the signal variance, P_k is the mean spectrum of the background noise at the frequency k, and the $\Rightarrow$ indicates "is distributed as." This relationship was recently confirmed in a theoretical framework by Ge (2007), especially in the case of Morlet function as the mother function.

Since the wavelet power spectrum in the spatiotemporal case is also defined by the square of WT as in the 1D case, it is natural to think that its distribution follows a χ_2^2 distribution just as in the 1D counterpart, namely

$$\frac{P_w(b, \tau; a, c)}{\sigma^2} \Rightarrow \frac{1}{2} P_k \chi_2^2. \quad (14)$$

Then the problem reduces to the estimation of the background spectrum and the degree of freedom to assess the statistical level of STWT. It may need substantial effort to develop a way to estimate the background spectrum in the spatiotemporal case based on a theoretical framework. Unfortunately, such a method does not seem to exist so far. However, there is a hint in the estimation of the background spectrum for the zonal wavenumber–frequency power spectrum developed by Wheeler and Kiladis (1999). Their background power spectrum is obtained by smoothing the raw spectrum by taking a 1–2–1 average[1] in both wavenumber and frequency many times. This provides a very simple but practical way to estimate the background power spectrum. Using the similarities between the zonal wavenumber–frequency power spectrum and the STWT (since they are both expected to follow a χ^2 distribution), the background power spectrum is obtained in the same way as Wheeler and Kiladis (1999).

b. Discretization of STWT and treatment of data

Since the real data is neither continuous nor infinite, careful treatments should be made to compute WT numerically, including how to discretize the STWT and how to treat edge effects.

There are two ways to develop a discretized framework for computing the STWT numerically. One is the

---

[1] The 1–2–1 average is a three-point average with 1/4–1/2–1/4 weight.

discretized continuous WT, which does not comprise orthonormal functions and thus has much redundancy. The other is the discrete WT, which is basically designed to constitute an orthonormal basis and thus has no redundancy. Although the discrete WT needs less computational resources owing to its nonredundancy feature, we employ the discretized continuous WT because of the good character of the quality of reconstruction and the stability with respect to perturbation by noise (Antoine et al. 2004). As in Torrence and Compo (1998), scale a is discretized as $a = a_0 2^{j\delta_j}$, $j = 0, 1, \ldots, J \in \mathbf{Z}$, and a_0, $\delta_j \in \mathbf{R}$ in which a_0 is the smallest resolvable scale. Let δx and δt be the sampling interval in x and t, and Nx and Nt be the number of samples in x and t. From the relationship between wavelet scales and Fourier wavelengths (C4), it is apparent that a reasonable selection would be $a_0 = (2\pi)^{-1}\sqrt{k'_M \omega'_M}\sqrt{\delta x \delta t}$ and $J = \delta j^{-1}$ $(\log_2\sqrt{NxNt} - 1)$ to cover all resolvable scales of the dataset. Similarly the speed tuning parameter is discretized as $c = c_0 2^{q\delta_q}$, $q = 0, 1, \ldots, Q \in \mathbf{Z}$, $c_0, \delta_q \in \mathbf{R}$. Also from (C5), one would take $c_0 = 2\delta x k'_M (Nt\delta t \omega'_M)^{-1}$ and $Q = \delta q^{-1}(\log_2 NxNt - 2)$. Note again that the STWT is computed in the Fourier space using (3) by means of the fast Fourier transform.

Another issue—the consideration of the edge effects—is simply handled by "padding" enough zeros to a power of 2 at the end of the data in both directions so that the end of the data is not polluted from the other end of the data. This is one of the popular techniques even in wavelet analysis (Strang and Nguyen 1996). Of course, excluding information from the analysis, for example, to judge the global wavelet scalogram based on the cone of influence consideration (e.g., Torrence and Compo 1998) tends to be more conservative. However, it is not appropriate in this case because the MJO component cannot be resolved due to the limitation of the longitudinal extent of the data.

c. Graphical representation of the wavelet power spectrum

We finish this section by considering how to display the wavelet power spectrum. With the STWT, the information about energy distribution is obtained at each grid point (b, τ) as a function of (a, c) as in the scalogram (7). There are thus two parameters (a, c) to examine the energy distribution at a given space and time (b, τ) or the overall energy distribution as a global wavelet scalogram (9). From its definition, it is natural to display its power spectrum in terms of those parameters. For instance, a is taken as the y axis and c as the x axis. It is the natural representation of the wavelet scalogram and may be used for a wide variety of applications in general. In contrast, a representation in zonal wavenumber–frequency space

is more convenient when dealing with signals in the tropics since we have a known equatorial wave theory that shows the dispersion relation of equatorial waves as a function of zonal wavenumber and frequency (Matsuno 1966). In fact, a substantial part of tropical convection is related to the equatorial waves (e.g., Hayashi 1982; Takayabu 1994; Pires et al. 1997; Wheeler and Kiladis 1999), the so-called convectively coupled equatorial waves (Kiladis et al. 2009).

Since this study has two purposes—providing an introduction to the STWT and discussing its application to the multiscale structure of MJO—we will provide the two types of graphical representations mentioned above in some cases. In representations, the relationship between (a, c) and a pair of zonal wavenumber and frequency (appendix C) is used to relate them.

4. Analysis of an ideal signal

To illustrate the application of STWT, we consider an ideal signal, $f(x, t)$, which comprises five harmonic propagating waves with different wavenumber and frequency, and their amplitudes vary with longitude:

$$\begin{aligned} f(x, t) = (0.5 + \sin k_0 x)[&2\cos(k_1 x + \omega_1 t) \\ &+ 0.5\cos(k_2 x - \omega_2 t) + 0.5\cos(k_3 x - \omega_3 t) \\ &+ 0.5\cos(k_4 x - \omega_4 t) + 0.5\cos(k_5 x - \omega_5 t)], \end{aligned}$$
(15)

where the zonal wavenumbers $k_0 = 1$, $k_1 = 2$, $k_2 = 10$, $k_3 = 20$, $k_4 = 40$, and $k_5 = 80$ and the corresponding periods $(T_n = 2\pi/\omega_n)$ $T_1 = 45$, $T_2 = 15$, $T_3 = 5$, $T_4 = 2$, and $T_5 = 1$. The time–longitude diagram of the ideal signal (15) is shown in Fig. 1a. While this is an ideal signal, the selection of both zonal wavenumber and period was based on the observational evidence that the tropical disturbance may consist of the MJO, quasi-biweekly oscillation (e.g., Chen and Chen 1993), synoptic scale (e.g., Reed and Recker 1971), quasi-two-day mode (e.g., Takayabu et al. 1996), and diurnal cycle (e.g., Kikuchi and Wang 2008). The longitudinal variations of the amplitude mimic the modulation of the climatological sea surface temperature (SST) variation (warm pool and cold tongue) on equatorial convective activity. Because this signal has neither trend nor noise and is completely periodic in time and space, some techniques such as zero-padding, tapering, and normalization by background spectrum were not employed in computing the power spectrum.

Figure 2 shows the natural representation of the global wavelet scalogram (9). Concentrations of energy are found where they are expected from (15). One of the merits of
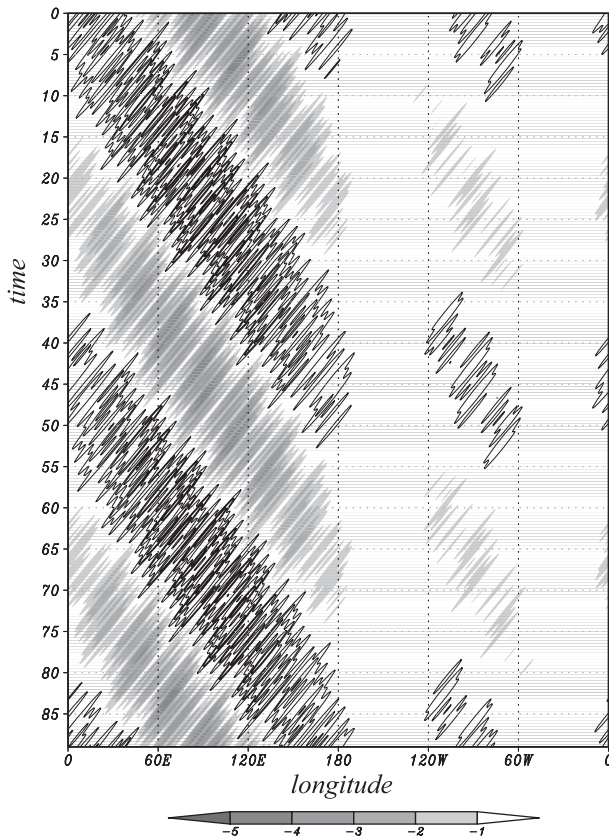
FIG. 1. Time–longitude section of an ideal signal represented by Eq. (15). Positive values are contoured and negative values are shaded; the contour interval is unit.

FIG. 2. Natural representation of global wavelet scalogram (averaged over the entire region) of the ideal signal. The spectrum is normalized by $a^3 c$. The lines that go down from the left to the right in the region of westward propagating signals correspond to best projected period (day); those that go up correspond to the best projected zonal wavenumber based on Eqs. (C4) and (C5). Contour interval is 0.01.

this representation lies in the readiness to identify the propagation direction by analyzing separately with both signs of k'_0, phase speed, wavelength, and period of all the components of a given signal.

The representation of the global wavelet scalogram in zonal wavenumber–frequency space (Fig. 3a) can be conveniently compared to the result obtained from the conventional Fourier-based zonal wavenumber–frequency power spectrum (e.g., Hayashi 1982) (Fig. 3b): both provide anticipated energy concentrations at the corresponding components of the signal. However, the power distribution in the STWT shows a slightly diffusive feature, which is expected from the definition of the STWT in spectral space (3). The diffusiveness, however, does not matter much and in some cases it could be desirable since it is considered to have a larger number of effective degrees of freedom (EDOFs) owing to the process of smoothing the spectrum (3). In conclusion, the global wavelet scalogram yields features consistent with the conventional wavenumber–frequency spectrum, so we can be sure that the overall spectrum characteristics are the same no matter which method is used.
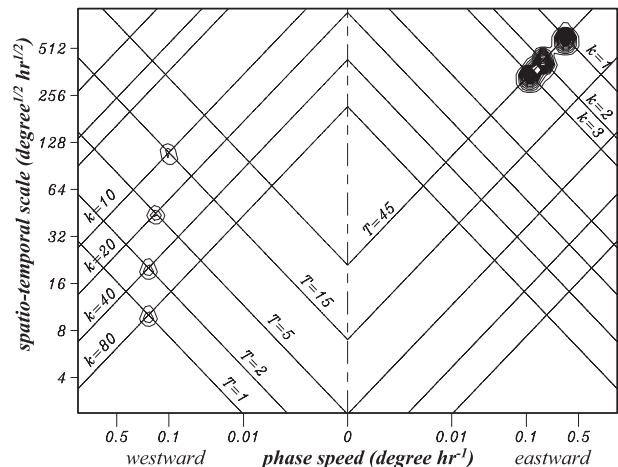
5. Multiscale structure of MJO: Nakazawa's case revisited

In the following sections, we examine the case that was first studied by Nakazawa (1988) as a real example of multiscale structure of the MJO. The data that we use are the same as in Nakazawa (1988), which are the *Geostationary Meteorological Satellite* (*GMS*) infrared data with horizontal resolution of 0.25° latitude × 0.25° longitude and a temporal resolution of 3 h. The data measures the temperature at the top of the clouds and thus well reflects deep convective activity in the tropics. The data cover the entire western Pacific and eastern Indian Oceans (60°S–60°N, 80°E–160°W). Due to the limited data coverage, zonal wavenumber 3 is the largest resolvable scale. The data period that we analyzed runs from 1 May through the end of July 1980. Since a few data values are missing, a linear interpolation in time was used to complete the time series so that a Fourier transform can be applied. Specific values of several parameters used in the STWT calculation, discussed in section 3, are summarized in Table 1.

a. STWT global wavelet energy spectrum (global scalogram)

First, we show the STWT global wavelet scalogram (an integrated wavelet power spectrum) in Fig. 4, which synthesizes the equatorial wave activity associated with the Nakazawa case. Similar to Wheeler and Kiladis's (1999) analysis, the data were decomposed into equatorial symmetric and antisymmetric component in accordance
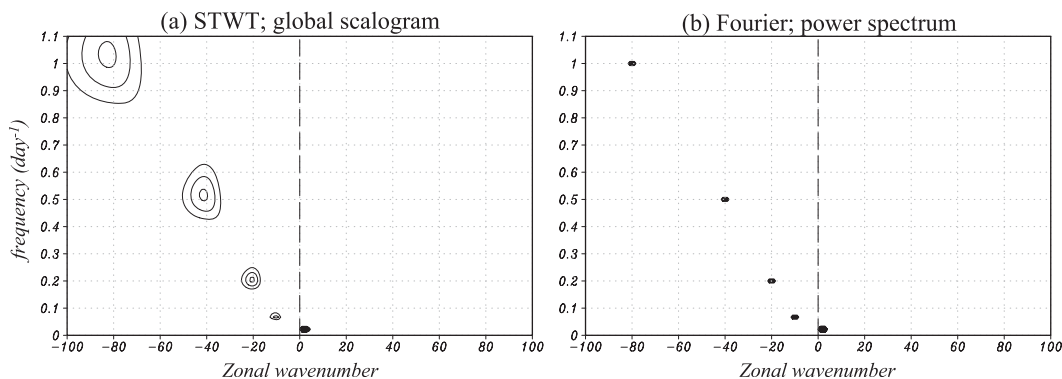
FIG. 3. Analysis of the ideal signal: (a) global spatiotemporal wavelet scalogram represented in zonal wavenumber–frequency space and (b) Fourier-based zonal wavenumber–frequency power spectrum. The wavelet scalogram is normalized by $a^3 c$. Contour interval is 0.01.

with the equatorial wave theory (Matsuno 1966). The most noticeable feature is a heavy concentration of energy at the planetary scale (wavelength 5000 to 14 000 km) in the eastward propagating signals of the symmetric component (Fig. 4a). Its eastward propagating speed has a wide range from $\sim$2 to 20 m s^{-1}. Based on the previous findings, they comprise two different components, the slow eastward propagating MJO ($\sim$8 m s^{-1}) and the fast eastward propagating signal (10$\sim$20 m s^{-1}) corresponding to moist Kelvin waves (Takayabu and Murakami 1991). In addition, the Kelvin wave component also has small spatiotemporal scale up to 2000 km and a non-dispersive feature (the phase speed is independent of the zonal or temporal scale). Energy concentrations are also found in the region of westward propagating signals in the symmetric component. The largest organized signal is related to $n = 1$ Rossby waves (labeled R), which has a zonal wavenumber of $\sim$6 ($\sim$7000 km) and westward phase speed of $\sim$7 m s^{-1}, similar to the convectively coupled Rossby wave (Kiladis and Wheeler 1995). Note that n stands for the meridional mode number of equatorially trapped waves (Matsuno 1966). Another notable signal is located at small scales with zonal wavelength <5000 km and period <3 days (labeled WIG), having a phase speed of about 15–30 m s^{-1}, which is associated with $n = 1$ westward propagating inertio-gravity waves (Matsuno 1966). Between the signals of the Rossby and the WIG waves, there is another signal with period $\sim$4 days, which may be classified as a tropical depression (TD)-type disturbance (e.g., Takayabu and Nitta 1993).

In contrast, there are only a few signals found in the antisymmetric component (Fig. 4b). The most prominent signal exists at the planetary scale in the region of eastward propagating signals. It has a very fast eastward phase speed of up to 50 m s^{-1} and is anticipated to be the $n = 0$ eastward propagating inertio-gravity (EIG) wave (Wheeler et al. 2000). Another signal can be found

in the region of westward propagating signals. It has a period $\sim$5 days and is also expected to be a TD-type disturbance (Wheeler and Kiladis 1999).

b. Comparison of the STWT power spectrum and the Fourier-based zonal wavenumber–frequency spectrum analysis

We have demonstrated how the STWT works in real data analysis and have shown that it is able to detect the variety of convective coupled equatorial wave signals. In light of the theoretical dispersion diagram of Matsuno (1966), a more convenient way to represent the equatorial waves is in zonal wavenumber–frequency space. Figure 5a shows the STWT global scalogram in zonal wavenumber–frequency space, which is compared with the Fourier-based zonal wavenumber–frequency power spectrum developed by Wheeler and Kiladis (1999) (Fig. 5b).

As expected, use of the zonal wavenumber–frequency diagram makes it easier to relate the signals to various types of equatorial waves as it can be directly compared with the Matsuno (1966) dispersion diagram (Fig. 5a). The MJO, Kelvin waves, $n = 1$ WIG waves, $n = 1$ Rossby waves, and TD-type disturbances are easily identified in the symmetric component and $n = 0$ EIG waves and TD-type disturbances in the antisymmetric component. The characteristics of those waves reflect equatorial Kelvin waves with zonal wavelengths $\sim$3000 km and periods 5$\sim$25 days, WIG waves with wavelengths 1000$\sim$5000 km

TABLE 1. Parameters of STWT calculation: N'_x and N'_t are the numbers of samples in x and t after zero–padding.

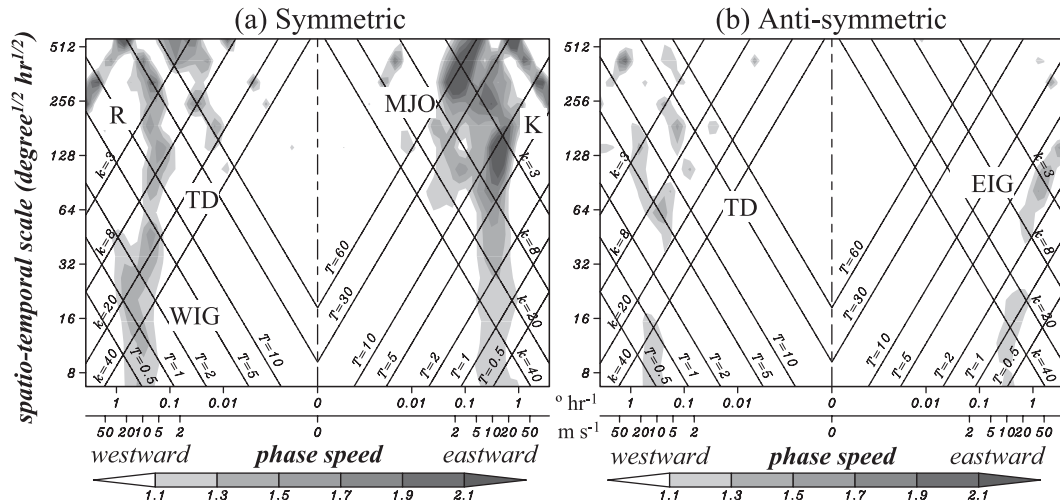| Name							
a_0	δ_j	J	c_0	δ_q	Q	N'_x	N'_t
Value 1.677	0.4	21	2.29×10^{-4}	0.45	35	2^{10}	2^{11}

(a) Symmetric   (b) Anti-symmetric

FIG. 4. Natural representation of global wavelet scalogram (10°S–10°N, 80°E–160°W) normalized by the background spectrum as a function of zonal phase speed (abscissa) and scale (ordinate): phase speed labeled in (top) ° h^{-1} and (bottom) m s^{-1} on the equator. The background spectrum is computed by taking a 1–2–1 average 10 times in both abscissa and ordinate directions. Lines going down from the left to right in the region of westward propagating signals correspond to the best projected period (day); those going up correspond to the best projected zonal wavelength (km) based on Eqs. (C4) and (C5).

and periods of 0.5~3 days, and mixed Rossby–gravity (MRG) and EIG waves with wavelengths 3000~ 40 000 km and periods of 1.5~10 days. In addition, the MJO signal, which does not fall in any dispersion curves of the equatorial waves at low zonal wavenumber and low frequency, is characterized by zonal wavelength ~5000 km and period 25~90 days.

As a comparison, Fig. 5b shows the Wheeler and Kiladis (1999) zonal wavenumber–frequency power spectrum derived from the Fourier transform. The methodology used to derive the diagram strictly follows Wheeler and Kiladis (1999). Note that we also taper the data to both ends in zonal direction because of the nonperiodic nature of the data. Obviously, the STWT and Fourier-based zonal wavenumber–frequency analysis yield similar wavenumber–frequency power spectra. However, the appearance of the STWT power spectrum is much smoother than the Wheeler and Kiladis spectrum: this is expected from the discussions in section 4 because the global wavelet scalogram has a larger number of EDOFs compared with the zonal wavenumber–frequency analysis. The large EDOF is a good property to detect systematic and significant signals, especially with short-record data. This smoothed feature of the wavelet spectrum is also consistent with the study of 1D WT by Torrence and Compo (1998). In the end, we can conclude that the global wavelet scalogram yields a quite consistent spectrum with that obtained from the zonal wavenumber–frequency analysis, and the STWT has potential advantage of detecting significant signals owing to its diffusive nature,

especially for short-record data. Moreover, the consideration of the statistical level made in section 3a seems to work reasonably well.

c. Multiscale structure of the MJO

The multiscale structure of the tropical convection associated with Nakazawa's MJO case is examined in this subsection. To begin, we classify disturbances into several components using (5) on the basis of the spectral features of the global wavelet scalogram of STWT (Fig. 5) so that we can examine how a given component is related to the other components. The components that we extracted are the MJO, Kelvin, WIG, equatorial Rossby waves, and MRG and EIG waves. As shown in Fig. 5, the areas of each subdomain D never overlap. With this "filtering" about 40% of variance, which includes background noise, can be explained by the sum of each mode (Table 2). Note that the variance contribution of each mode can be obtained by use of (8).

Figure 6 shows a suite of Hovmöller diagrams of *GMS* infrared data averaged between 0° and 5°N for using the original data by subtraction of the May–July mean and linear trend (Fig. 6a) and using STWT filtering for each type of disturbance. At first glance, in Fig. 6a one may notice an active convective period starting from late May and ending in mid-July. During that period Nakazawa (1988) identified four super cloud clusters, labeled "A" to "D" in Figs. 6a. Figures 6b–f show the five components of the decomposed convective activity during the 3-month period; they together reveal the multiscale
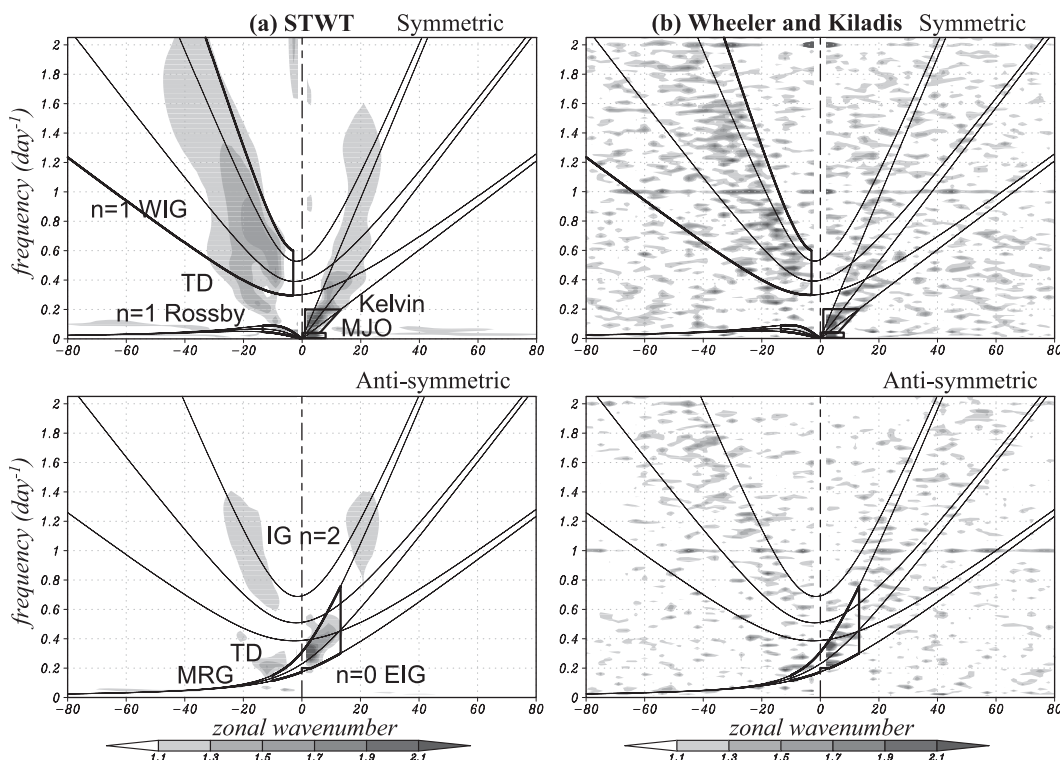
FIG. 5. Zonal wavenumber–frequency power spectrum for the (top) equatorial symmetric and (bottom) anti-symmetric components of infrared data signals in the equatorial region between 10°S and 10°N in the *GMS* domain (80°E–160°W). The power spectrum was computed by means of (a) spatiotemporal wavelet transform and (b) conventional space–time Fourier transform. The power spectrum was normalized by the background spectrum obtained as in Wheeler and Kiladis (1999). For reference, the values of 1.1, 1.3, and 1.5 meet the 90% significance level with effective degrees of freedom 340, 40, and 15, respectively. Each curve is a dispersion curve obtained from an equatorial beta plane with equivalent scale height of 5, 15, and 50 m.

structure of the MJO. It is evident that most westward propagating systems seen in Fig. 6a are the WIG waves (Fig. 6b). The four SCCs identified by Nakazawa in Fig. 6a are associated with convectively coupled equatorial Kelvin waves (Fig. 6c). The MJO component (Fig. 6d) represents a slow eastward propagating component that has slower phase speed compared with the Kelvin waves. The westward propagating equatorial Rossby and MRG waves and the eastward propagating EIG waves are mainly seen in the western Pacific (Figs. 6e and 6f) and do not appear to be major players interacting with either MJO or Kelvin waves: thus they are ignored in the following discussions.

6. Differences and relationships between the moist Kelvin wave and MJO

a. Different meridional structure of the Kelvin wave and MJO

Before moving on to study the relationships among different components, we examine the horizontal structures

of the Kelvin wave and MJO to ensure that they are reasonably separated. It is well known that they have different horizontal structures in terms of convection and circulation (e.g., Hendon and Salby 1994; Straub and Kiladis 2003b). Figure 7 shows a composite horizontal structure of filtered infrared data for each component. The composite is an average of collected data along the phase lines of the Kelvin wave and MJO defined in Figs. 6c and 6d.

As expected, they show different structures clearly. The Kelvin wave has a monopole structure with maximum amplitude in the Northern Hemisphere at ~2.5°N (Fig. 7a). Similar deviation of the Kelvin-wave-related convection from the equator during boreal summer has been found in the previous observational studies (e.g.,

TABLE 2. Ratio of variance of each component to total variance.

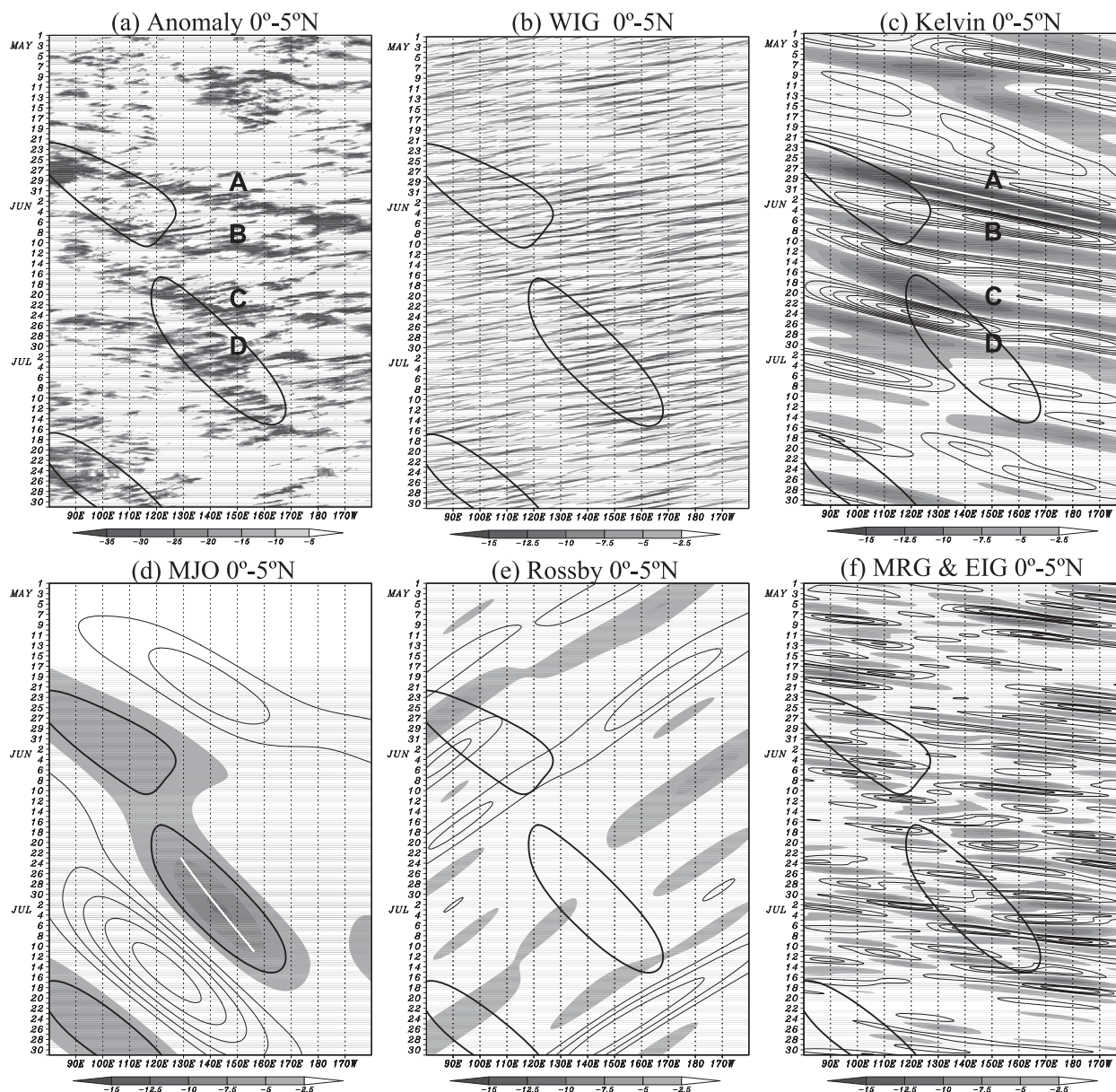|	Wave component					
	WIG	Kelvin	MJO	Rossby	MRG	Total
Ratio (%)	16	8	4	4	6	39

FIG. 6. Hovmöller diagram of *GMS* IR (K) averaged between 0° and 5°N of (a) the original data with the May–July mean removed and (b)–(f) its filtered components: (b) WIG waves, (c) Kelvin waves, (d) the MJO, (e) Rossby waves, and (f) MRG and EIG waves. Labels "A" to "D" in (a) and (d) are the same as the labels used in Fig. 1 of Nakazawa (1988), indicating the four super cloud clusters. White lines in (c) and (d) are phase lines along with the Kelvin wave and MJO, respectively, drawn with reference to their amplitudes, which will be used in the composite later (e.g., Fig. 7). The contour lines of the MJO at -5 W m^{-2} are superimposed by thick solid curves for reference.

Straub and Kiladis 2002, 2003b). This northward deviation is likely due to the northward shift of warm SST and the corresponding boundary layer moist static energy, as documented by Wang and Xie (1997).

On the other hand, MJO has a northwest–southeast-tilted convection anomaly in the Northern Hemisphere. This structure appears to be similar to the composite structure of OLR by Seiki and Takayabu (2007) in their western Pacific case derived with long-term data. They

studied the behavior of westerly wind bursts and made their composite based on the bursts. In their figure, at day 0 (corresponding to the phase that this study shows) a meridional elongated convective anomaly emerges, accompanying a coupled Kelvin–Rossby wave response at the surface (Wang and Rui 1990).

It is therefore plausible to think that the MJO and Kelvin waves are reasonably separable because they have different phase speeds and different horizontal structures
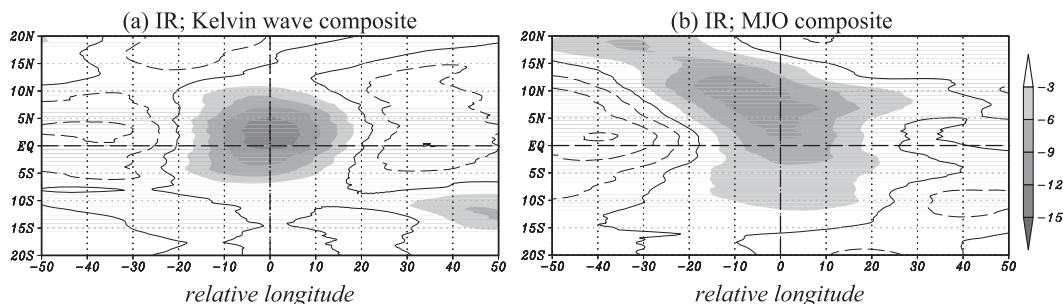
FIG. 7. Horizontal structures of the composite of infrared anomaly for the (a) Kelvin wave and (b) MJO components. Composite is constructed along the phase line shown in Figs. 6c and 6d, respectively. The x axis is relative longitude with reference to each phase line. Contour interval is 3 K; negative values are shaded.

of convection. In addition, it is expected that they have different accompanying circulation structures as well.

b. Relationship between the MJO and moist Kelvin waves

As seen in Fig. 6 and the discussion above, the convective activity associated with the moist Kelvin wave and with the MJO seems to be well separated. The moist Kelvin wave component has a faster phase speed of $\sim$10–20 m s^{-1} compared with the slow phase speed of $\sim$2–8 m s^{-1} for the MJO (Fig. 4a). Four SCCs labeled "A" to "D" are clearly related to the moist Kelvin wave component (Fig. 6c).

Nakazawa (1988) postulated that the SCCs (or the Kelvin wave components) are embedded in a convectively active region of the MJO, and the MJO was visualized as an intangible envelope of convective region moving eastward at a slower phase speed than the SCCs. However, we would like to offer a somewhat different view based on the STWT analysis. The results in Fig. 6 suggest that the MJO itself may be a substantial, organized convective system rather than an intangible envelope of an eastward-moving convectively active region. In fact, there are organized convective systems in association with the MJO component. While the moist Kelvin wave and MJO sometimes coexist, an obvious example of the MJO that does not involve Kelvin wave is seen in early July along the white color line in Fig. 6d. Note that the corresponding eastward phase speed is approximately 2 m s^{-1} in this case, which is a little slower than the typical phase speed of the MJO of $\sim$5 m s^{-1} (e.g., Hendon and Liebmann 1994).

Supposing that the MJO and Kelvin waves are different "animals," do they relate to each other? In a statistical sense, Straub and Kiladis (2003a) found that the relationship between the MJO (which they called the boreal summer intraseasonal oscillation) and Kelvin wave activity varies with the MJO phase. When an enhanced convective region associated with the MJO lies in the equatorial eastern Indian Ocean, the enhanced Kelvin wave activity collocates with the MJO but, when the enhanced convective region shifts to the Maritime Continent or western North Pacific, the enhanced Kelvin wave activity exists to the east of the enhanced convective region.

Figure 8 shows a Hovmöller diagram of a local wavelet scalogram anomaly of the Kelvin wave component, which corresponds to the variability of the Kelvin wave activity, together with the enhanced convective region of the MJO. When an enhanced convective region associated with the MJO is located in the Indian Ocean (around late May), an enhanced Kelvin wave activity somewhat collocates. However, excitement of Kelvin waves does not seem to occur exclusively in the active convective region of the MJO; rather, it seems to occur constantly in the active period of convection in the eastern Indian Ocean from late May to late June. When the enhanced convective region of the MJO is located over the Maritime Continent around early June, the Kelvin wave activity (local wavelet scalogram) is well enhanced (more than one standard deviation) to the east in the western Pacific, consistent with the results of Straub and Kiladis (2003a).

What we would like to emphasize here is that the STWT provides a convenient and intuitive way to estimate the energy of a given disturbance represented by the local wavelet scalogram that corresponds to a wave packet of a given wavelet function. This estimation is mathematically well structured, and we need no concern to go though some complicated treatment to estimate the wave packet of a given component such as by applying a bandpass filter (Matthews and Kiladis 1999) or taking a lead–lag composite (Straub and Kiladis 2003a) to a square root of a given disturbance. In addition, the STWT gives a better opportunity to examine how the characteristics of a Kelvin wave, such as phase speed, are modified by the MJO. The more detailed analyses discussed above provide insight into some aspects of
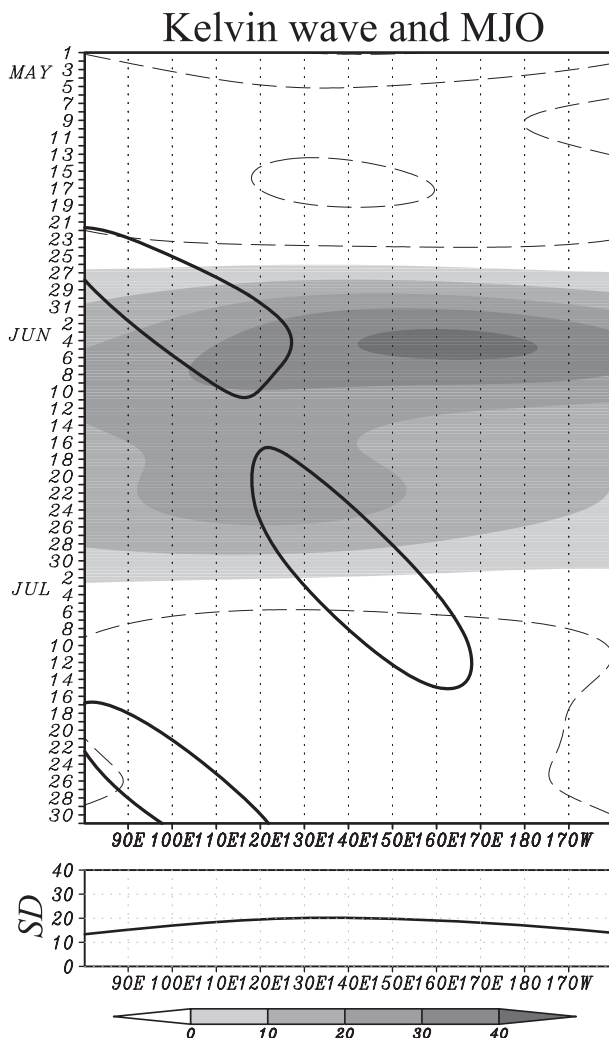
Kelvin wave and MJO

FIG. 8. Hovmöller diagram of local wavelet scalogram anomaly (K^2) averaged between 0° and 5°N that corresponds to the Kelvin wave component defined in Fig. 5. The anomaly is defined as deviation from the May–July mean at each point and the linear trend is also removed. Positive (negative) values are shaded (contoured). Thick solid lines indicate contour lines at -5 K for MJO. The lower panel shows the standard deviation of the local wavelet scalogram at each longitude.

interaction between Kelvin waves and MJO and understanding the complex behavior of Kelvin waves (e.g., Roundy 2008).

7. Modulation of WIG waves by the MJO and moist Kelvin waves

In this section, additional examples are shown to demonstrate how the STWT can be conveniently used to reveal relationships between the WIG and Kelvin waves and between the WIG waves and the MJO.

a. Modulation of WIG wave activity (energy)

Figure 9 shows the Hovmöller diagrams of the WIG wave activity in terms of a local wavelet scalogram (10) along with the active convective regions of Kelvin waves and the MJO. From Figs. 9a and 9b, it is evident that the WIG wave component is strongly modulated by both Kelvin waves and the MJO; that is, within the active convective area of either the Kelvin wave or MJO, the activity of WIG waves is enhanced (amplitude is around one standard deviation). This confirms the results of Nakazawa (1988), who showed that the actual convective system develops in the form of westward-moving cloud clusters. The WIG wave component accounts for a large portion of the variance of ~16% (Table 2) and has been identified as the theoretical counterpart of a cloud cluster (Takayabu 1994).

To provide a more robust feature of how WIG wave activity is modulated by Kelvin waves and the MJO, we show a composite of local wavelet scalograms of WIG wave components along the Kelvin wave and the MJO in Fig. 10. The procedure of making the composite is the same as in Fig. 7. It is interesting to note that the horizontal patterns of local wavelet scalograms of WIG waves associated with the Kelvin wave and MJO are much different. The local wavelet scalogram within the Kelvin wave is concentrated in the center of the convective area (Fig. 10a). In contrast, the local wavelet scalogram has a large anomaly to the east of the convective center within the MJO (Fig. 10b). This feature indicates that the MJO is preconditioned by active WIGs to the east of the major convective area, while the moist Kelvin waves do not. This result is consistent with the previous studies, which found that the MJO has a preconditioning stage to the east of the major convective area (Maloney and Hartmann 1998; Kiladis et al. 2005) that consists of different cloud types—stratocumulus and congestus clouds (Johnson et al. 1999; Kikuchi and Takayabu 2004)—and the Kelvin waves do not have this preconditioning stage (e.g., Straub and Kiladis 2003b).

b. Modulation of WIG waves propagation and wavelength

Figure 11 shows a typical case of how convection develops in association with Kelvin waves and the MJO. Figure 11a shows the same case analyzed in Nakazawa (1988). As expected, our analysis yields an internal structure similar to that found by Nakazawa—that is, there are westward-moving clusters with zonal wavelengths of a couple of or several thousand kilometers and their lifetime is 1~2.5 days. The mature convections move eastward by switching from one westward-moving cluster to the next. The WIG waves in the MJO also have similar
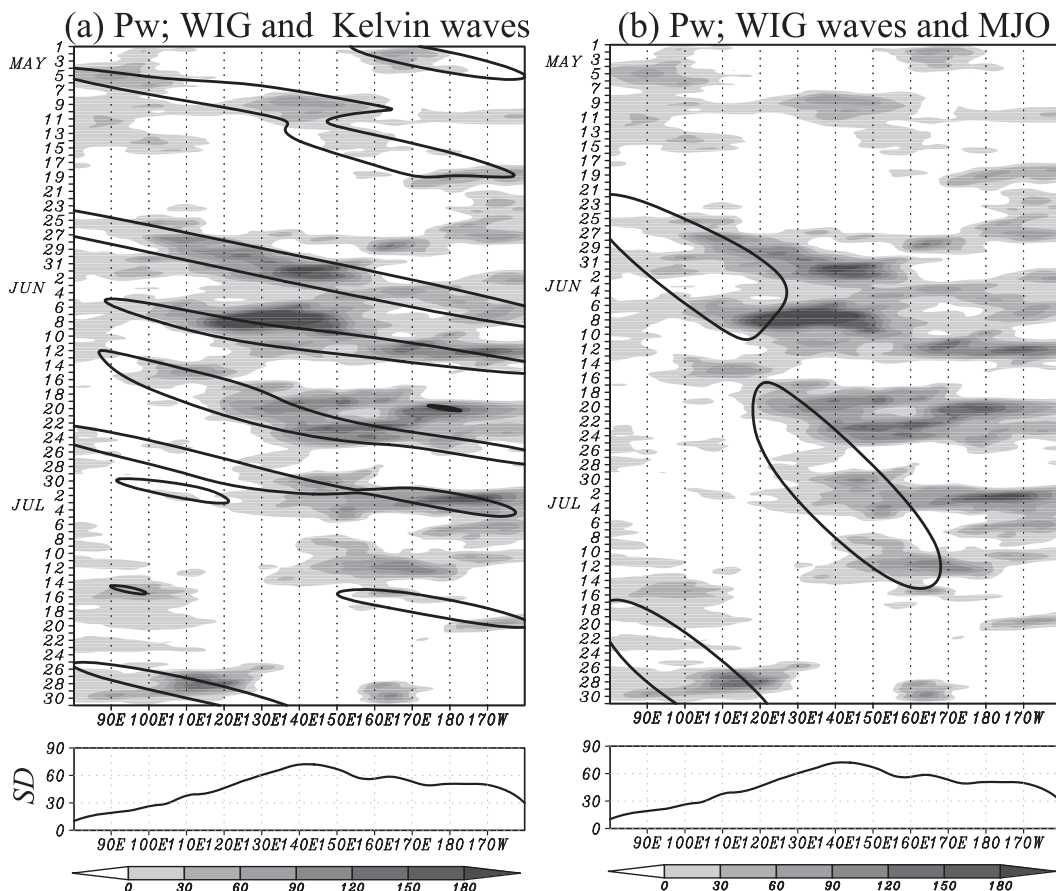
FIG. 9. As in Fig. 8 but for WIG waves. Thick solid lines indicate contour lines at −5 K of infrared data for the (a) Kelvin waves and (b) MJO component.

organized structure, while the zonal wavelength of WIG waves seems somewhat shorter (Fig. 11b).

To examine in more detail how the characteristics of embedded WIG waves are different between Kelvin waves and the MJO, we take advantage of the STWT's unique capability of detecting the local zonal wavenumber and frequency of a nonstationary wave. Figure 12 shows

the temporal variations of the most predominant local zonal wavenumber and frequency of the embedded WIG waves in the Kelvin wave and MJO along with those of filtered infrared data. In both cases, westward propagating disturbances are enhanced in the active convection region of the Kelvin wave and MJO (Figs. 12a and 12b), while westward propagating disturbances appear
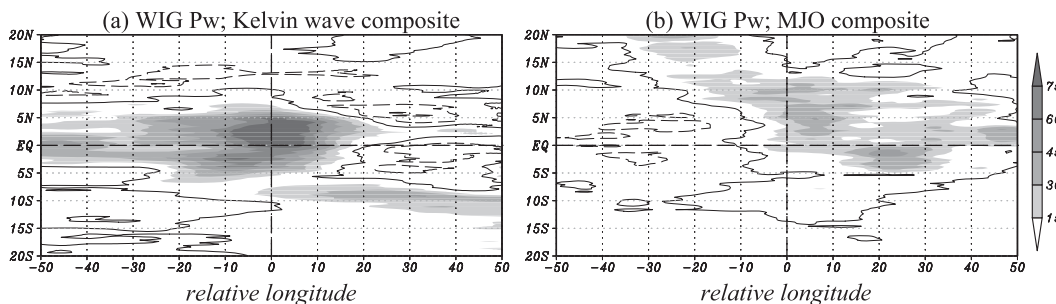

FIG. 10. As in Fig. 7 but for local wavelet scalogram of WIG waves anomaly. Contour interval is 15 K^2. Positive values are shaded. Given that x axis is relative longitude with reference to each phase line, the convective center of each component is located at 0° in the longitudinal direction.

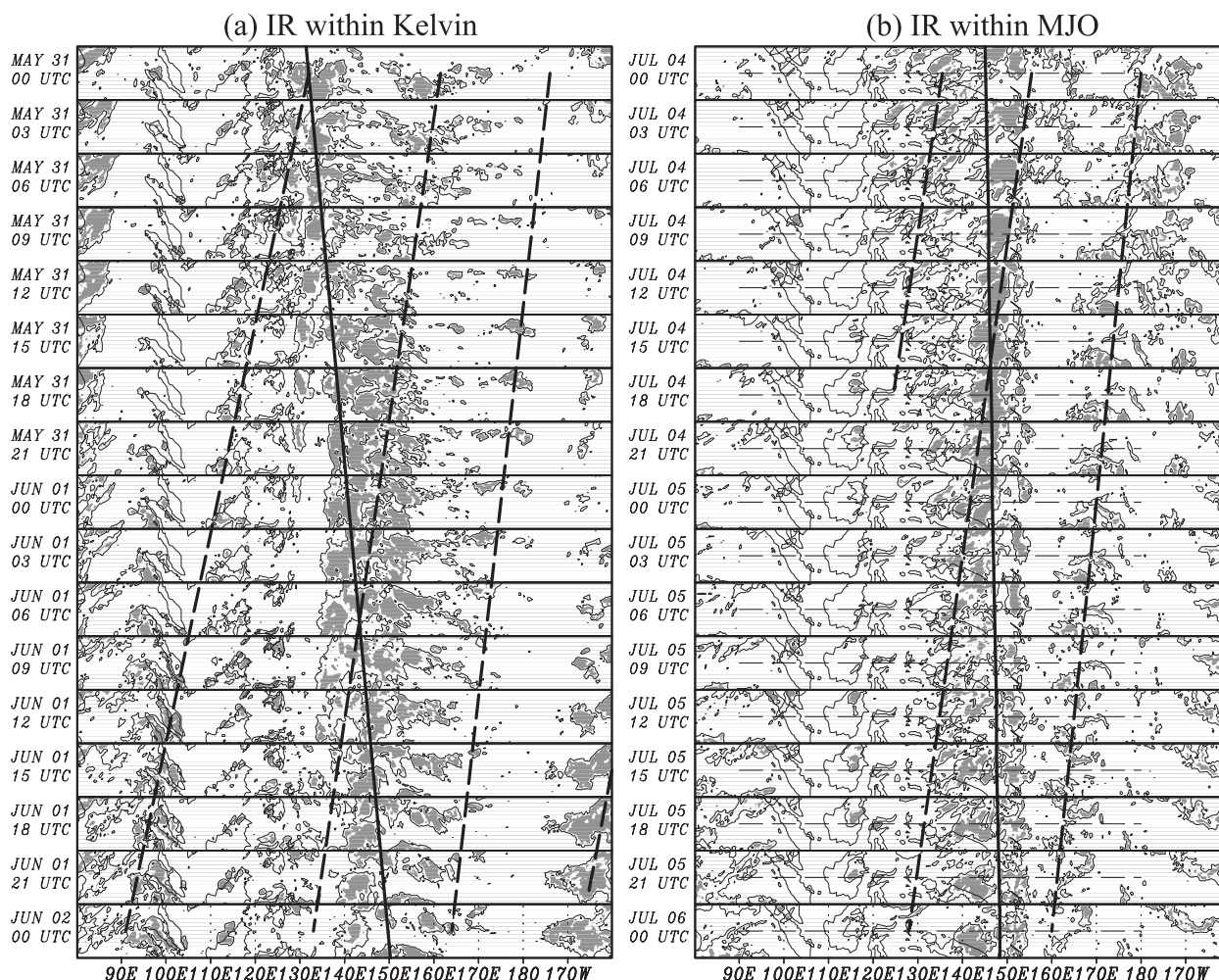## (a) IR within Kelvin   (b) IR within MJO

FIG. 11. Hovmöller diagram of infrared data between (a) the equator and 10°N from 0000 UTC 31 May to 0000 UTC 2 Jun and (b) 5°S and 5°N from 0000 UTC 4 Jul to 0000 UTC 6 Jul. Values less than 225 K are shaded; contour interval is 50 K. Dashed lines indicate the phase of low-frequency WIG waves drawn based on the Hovmöller diagram of that component (not shown), and thick arrows indicate the phases of the major body of organized convection in association with the (a) Kelvin wave and (b) MJO components that correspond to the phase line in Figs. 6c and 6d.

more continuously within the Kelvin wave than within the MJO. The corresponding evolution of the WIG waves is seen in the predominant local zonal wavenumber and frequency in both cases (Figs. 12c–f). For both cases, there are two components of energy concentration in terms of local zonal wavenumber and frequency but where the energy concentration tends to occur is different between the Kelvin wave and the MJO. The concentration of energy is seen around wavenumbers 10 and 40 and frequency between 0.4 and 0.8 and greater than 1 in the Kelvin wave. In contrast, the energy concentration occurs around wavenumbers 18 and 30 and frequency less than 1 and greater than 1.2 in the MJO.

The suggested differences of WIG waves in terms of zonal wavenumber and frequency embedded within the

Kelvin wave and the MJO is confirmed by the composite power spectrum during the same period (Fig. 13). In Fig. 13, one can see that the most prominent energy concentration is located in the region outlined by the thick black curves in both the Kelvin wave and MJO. In addition, as this component is thought to play an important role in upscale feedback (to be shown later), we will focus on this component. This energy concentration region suggests that WIG waves within the Kelvin wave tend to have zonal wavelength of 3000~5000 km and periods ~2 days, while those within MJO tend to have zonal wavelength 2000~3000 km and period ~1.1 days. Thus, the WIG waves embedded in the Kelvin waves and MJO have a similar phase speed of about 15–30 m s^{-1}. We will call these WIG waves as the 1–2.5 days WIG waves for simplicity.
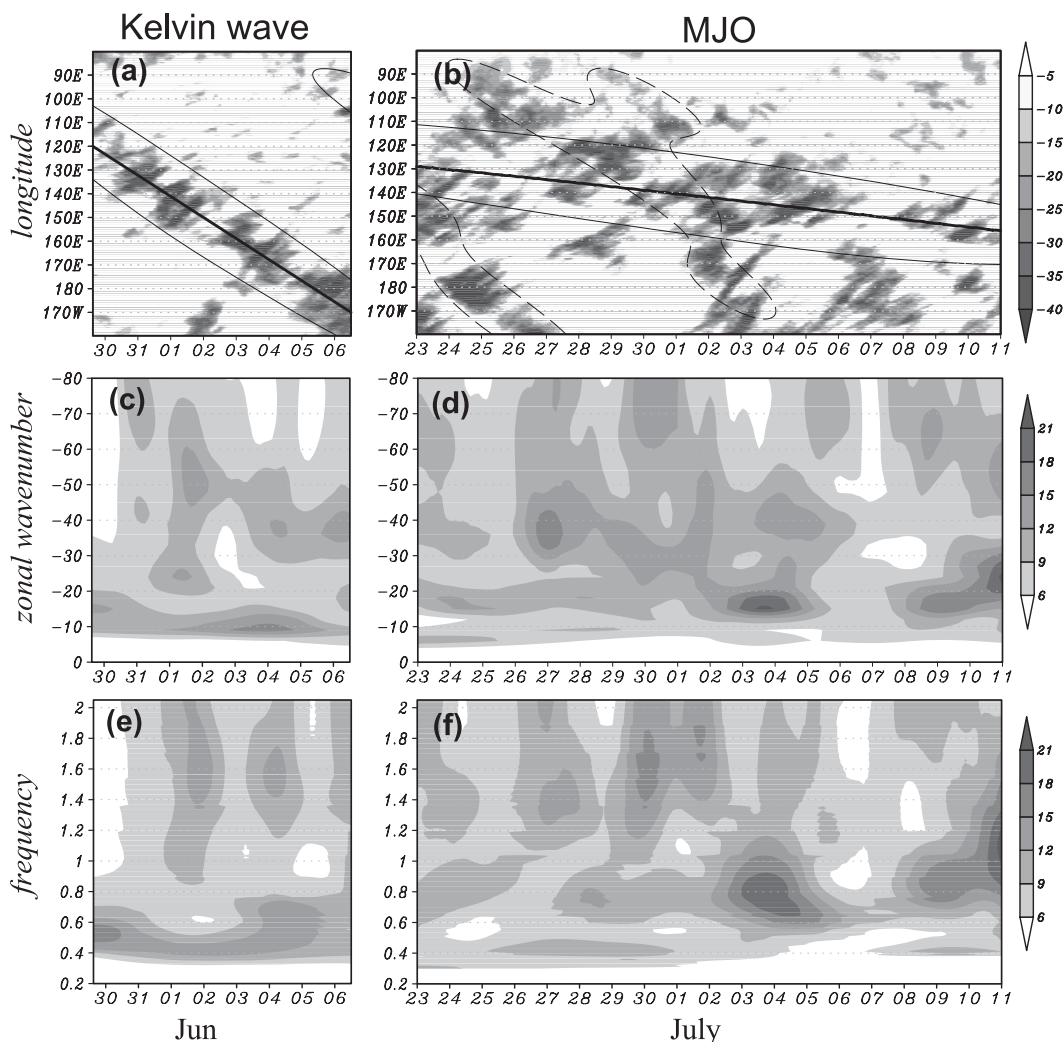
FIG. 12. Close examination of the behavior of WIG waves within the (left) Kelvin wave and (right) MJO. (top) Hovmöller diagram of infrared data. (middle), (bottom) Temporal variation of most significant spectrum peaks of WIG waves as a function of (middle) zonal wavenumber and (bottom) frequency averaged between the equator and 10°N. Note that the abscissa and the ordinate in Hovmöller diagram are reversed from earlier figures. (a),(b) Thick lines indicate the phase lines of the Kelvin wave and MJO, respectively, which correspond to the phase lines defined in Fig. 6. Thin lines are contour level of -5 W m^{-2} of the Kelvin and MJO components. Dashed line representing the Kelvin wave component of -5 W m^{-2} is superposed in (b). (c)–(f) No symmetric and antisymmetric separation is made to compute the power spectrum. The power spectrum is normalized by the background spectrum of the global wavelet scalogram. Note that the value of the normalized wavelet spectrum of 6.7 passes a significance test against background spectrum at 99% with an EDOF of 6.

One notable difference between the Kelvin wave and MJO is the different properties of the embedded WIG waves. What causes this difference? Since the scales between the WIG waves and Kelvin waves or MJO are well separated, the large-scale circulation produced by Kelvin waves or the MJO would act like part of the background field to WIG waves. Theoretical works suggest that any equatorial waves are more or less modulated by the presence of meridional or vertical shears (e.g., Wang and Xie 1996). Given that the moist Kelvin wave and MJO

are expected to have different large-scale circulations (see the discussion in section 6a), the convectively active region in association with an MJO component is expected to have stronger meridional and vertical shears due to the existence of Rossby wave response (e.g., Kiladis et al. 2005) than with the Kelvin wave component (e.g., Straub and Kiladis 2003b). It is therefore conceivable that either the joint meridional and vertical shear or one of them is responsible for making the difference. Further theoretical study will be necessary to elucidate the concrete processes.
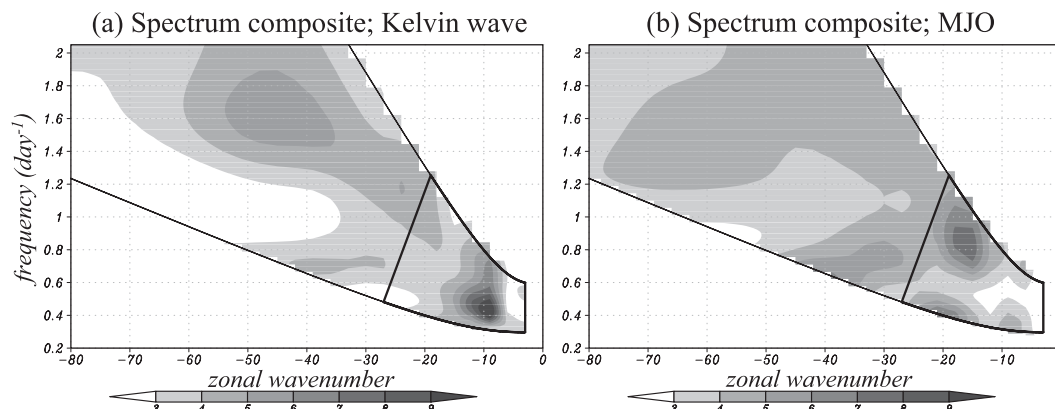
FIG. 13. Composite power spectrum of WIG waves with reference to the (a) Kelvin wave and (b) MJO averaged between the equator and 10°N. No separation between symmetric and antisymmetric is made. The thin line outlines the region of the WIG waves; the thick line indicates the region of the lower-frequency component of WIG waves. Note that the value of the normalized wavelet spectrum of 6.7 passes a significance test against the background spectrum at 99% with an effective degrees of freedom (EDOF) of 6.

8. Possible upscale feedback from WIG waves to the MJO and Kelvin waves

In this section we examine whether the collective activity of the 1–2.5-day WIG waves is able to affect the behavior of Kelvin waves and the MJO.

a. Relationship between convective bursts and the 1–2.5-day WIG wave component

To explain why we think the 1–2.5-day WIG waves are especially important in affecting the behavior of Kelvin wave and MJO, in Fig. 14 we show the Hovmöller diagrams of raw infrared data (contours) along with the path of the 1–2.5-day WIG waves (shades). Note that the 1–2.5-day WIG waves embedded in the Kelvin wave and MJO indeed have different behavior as suggested by the STWT power spectrum (Fig. 13): the 1–2.5-day WIG waves in the Kelvin wave have longer wavelengths (3000~5000 km) and periods of about 2 days, whereas those in the MJO have shorter wavelengths (2000~3000 km) and periods of around 1 day. In both the Kelvin wave and MJO components, the bursts of convection (as shown by the contours) appear to occur when the phase lines of the Kelvin wave (or MJO) and the 1–2.5-day WIG waves intersect. This result implies that the interaction between WIG waves and low-frequency Kelvin waves or the MJO may be instrumental in understanding the convective bursts associated with the low-frequency MJO and Kelvin waves. Thus, the WIG waves are not only modulated by low-frequency waves but also possibly play a role in sustaining the convective bursts associated with low-frequency disturbances.

b. A possible feedback of the embedded WIGs on MJO and Kelvin waves

Precipitation usually occurs in a mesoscale convective system with a lifetime of 2–3 days at most. One of the major roles of the WIG waves is supplying convective heating to their regulators (e.g., Haertel et al. 2008): the MJO and Kelvin waves. The collective effect would modify the structure of the Kelvin wave and MJO. Another major role that we suggest is the potential impact of the WIG waves on propagation speeds of the Kelvin wave and MJO.

Based on the results of Fig. 14, a schematic summary is presented in Fig. 15 along with the following discussion. From the considerations in the previous subsection, the 1–2.5-day WIG waves may play an important role in switching on the major convective region activity. Because the WIG waves embedded in the MJO have shorter wavelengths, the MJO should have more cloud clusters than Kelvin waves in a given period of time. In fact, more cloud cluster events take place in the MJO case than in the Kelvin wave case during the same period of time (Fig. 14). In other words, the MJO intersects with 1–2.5-day WIG waves more frequently than the Kelvin wave does. Since the release of latent heat or interaction with heating is one of the primary mechanisms that can slow down the phase speed of the moist Kelvin wave (Lau and Peng 1987; Wang 1988) or coupled Kelvin–Rossby wave packet–MJO type disturbance (Wang and Rui 1990), it is plausible that more frequent occurrence of the WIG waves (cloud clusters) would result in more latent heat release, thereby slowing down the propagation of the large-scale circulation associated with the MJO and moist Kelvin waves. In summary, an accurate

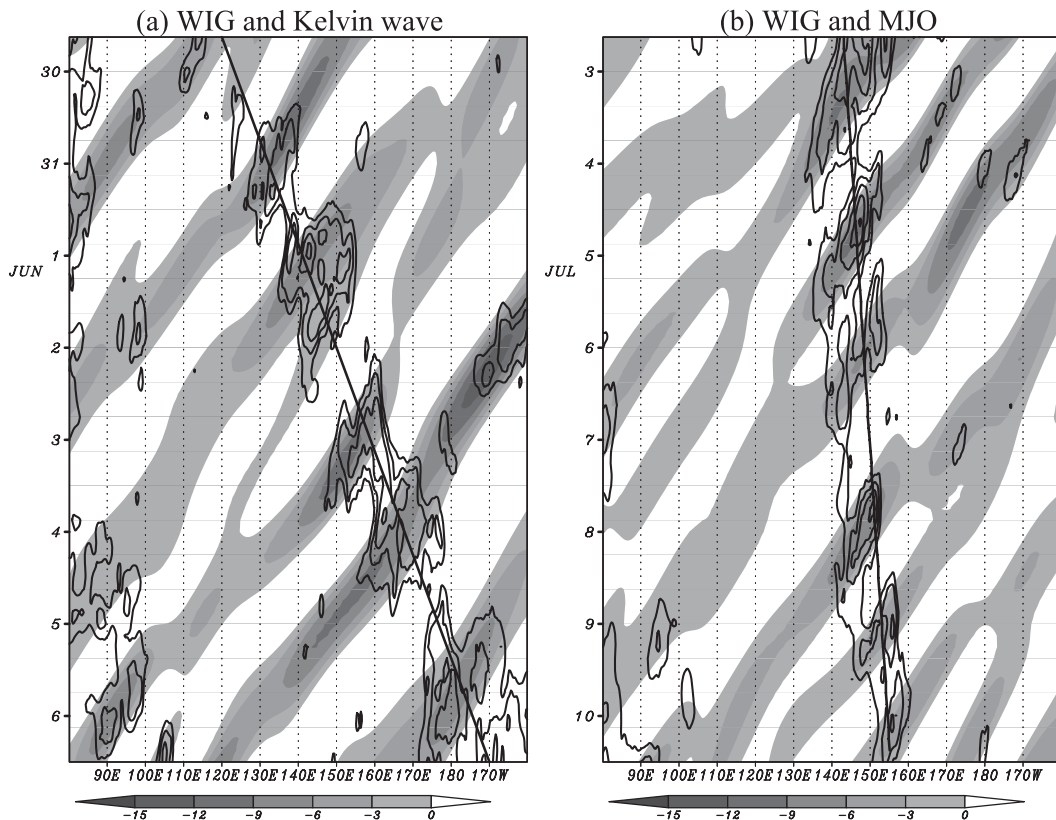## (a) WIG and Kelvin wave

(b) WIG and MJO

FIG. 14. Hovmöller diagram of lower-frequency components (1–2.5-day period) of WIG waves (shades) within (a) Kelvin waves averaged between 0° and 10°N and (b) the MJO averaged between 5°S and 5°N. Low infrared values (less than 250 W m^{-2}) of nonfiltered data are superposed as contour lines with contour interval 10 W m^{-2}. The reference phase lines are shown by thick lines correspond to those in Fig. 6.

documentation of the multiscale structure of both the MJO and Kelvin waves may be one of the key aspects toward a comprehensive understanding of the different slow phase speeds of the MJO and moist Kelvin waves.

9. Summary

a. Advantages and limitations of the STWT

It is shown that the STWT has the capability to display time–frequency localization; this enables us to study the behavior of nonstationary waves and multiscale behavior of tropical convection. The zonal wavenumber–frequency analysis based on the Fourier transform is a useful "spatiotemporal filtering" tool to isolate different disturbances, but it is difficult to examine multiscale interaction owing to its inability to deal with nonstationarity of the waves. The STWT is more useful in this regard. Figures 12 and 13 are good examples to show the local energy distribution as a function of space and time. Given that the global wavelet scalogram (integrated wavelet scalogram) yields quite consistent features with the Fourier-based

power spectrum, there is little doubt that the local energy distribution gives a reasonable snapshot or slice of the power spectrum. In addition, the global wavelet scalogram facilitates detection of systematic significant signals from the short-term data due to its diffusive feature. Because of its reconstruction capability, the STWT also provides a natural spatiotemporal filter.

However, the STWT is computationally more time consuming. It is clear from (3) that the Fourier transform in both time and space is required to calculate the STWT for the given scale and speed tuning parameter. This alone requires computational resources comparable to the conventional zonal wavenumber–frequency analysis based on two-dimensional Fourier analysis. Thus, computation of the global wavelet scalogram requires multiple times to cover the whole scales and speed tuning parameters. The computational time depends on how fine a scale interval and speed tuning parameter one takes. In this study, for instance, about 750 ($\sim$21 $\times$ 35) pairs of (a, c) (Table 1) for both positive and negative k_0 requires about 1500 times longer computational time in STWT than in the conventional method. It is therefore
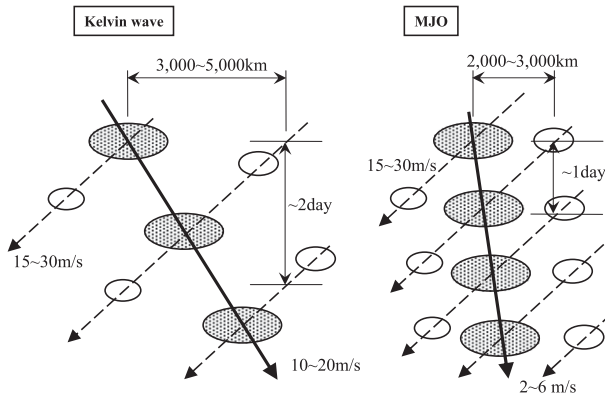
FIG. 15. Schematic diagram summarizing the multiscale structure of (left) Kelvin waves and (right) the MJO. Dashed arrows indicate WIGs; and solid arrows indicate phase lines associated with (left) Kelvin waves and (right) the MJO. Circles represent cloud clusters. Characteristic wavelength and period for WIG waves and phase speed for all components are also shown.

helpful to develop a discrete WT that has less redundancy and consequently requires less computational time while retaining some preferable features that the continuous WT has, such as the shift equivariant WT (e.g., Fournier 2000).

b. Scale interaction associated with the MJO

The ability of the STWT to reveal time–frequency localization greatly facilitates study of multiscale behavior and possibly the two-way scale interaction. The activity of the WIG waves is strongly modulated by both the Kelvin wave and MJO components. Specifically, the WIG waves tend to coincide with the most enhanced convective area of the Kelvin wave, whereas they are primarily enhanced to the east of the most convective center of the MJO. Another difference, which is an interesting new finding due to the advantage of the STWT, is the dissimilar behaviors of WIG waves embedded in the Kelvin wave and MJO. The low-frequency component (1–2.5-day period) of WIG waves has larger zonal wavelength and longer period in the Kelvin wave than in the MJO. A possible upscale feedback was discussed in section 8.

The results of the present analysis suggest that convectively coupled Kelvin waves and the MJO may be viewed as separate systems. Although they often coexist, their structures and propagation speeds are different. On the other hand, they are related: the Kelvin wave tends to be stronger to the east of the MJO when the enhanced convection associated with the MJO is located over the Maritime Continent. This feature is consistent with the previous statistical analysis results obtained by Straub and Kiladis (2003a). The relationship between

Kelvin waves and the MJO requires further examination with long-term data in order to address some important questions, such as how MJO interacts with the Kelvin waves.

This study shows how the STWT method works when examining the interactions among convectively coupled equatorial waves, but what we have done is limited. Further studies are needed to obtain more convincing conclusions; in particular, more cases should be examined in the future. In addition, the Rossby and MRG waves should be taken into account in order to make the discussion more complete.

APPENDIX A

Proof of the Resolution of the Identity (Reconstruction Feature)

In the present study, the continuous STWT was developed in a way similar to Torrence and Compo (1998). Since the continuous WT is redundant, we can choose an alternative function to obtain a reconstruction formula rather than use the wavelet function itself. One of the easiest ways is to take a delta function (δ) as in Farge (1992) or Torrence and Compo (1998). Consider the following integral:

$$I_1 = \int_0^\infty \frac{da}{a^2} \int_0^\infty \frac{dc}{c} \int_{-\infty}^\infty db \int_{-\infty}^\infty d\tau W(b, \tau; a, c)\langle \delta_{b,\tau}, g \rangle,$$

(A1)

where $\langle f, g \rangle = \int_{-\infty}^{\infty} dx \int_{-\infty}^{\infty} dt f(x, t) g^*(x, t) = \int_{-\infty}^{\infty} dk \int_{-\infty}^{\infty} d\omega \hat{f}(k, \omega) \hat{g}^*(k, \omega)$ represents the inner product of two dimensional functions: f and g. Here $\langle \delta_{b,\tau}, g \rangle$ can be represented in Fourier space as follows:

$$I_1 = 2\pi \int_0^{\infty} \frac{da}{a} \int_0^{\infty} \frac{dc}{c} \int_{-\infty}^{\infty} dk \int_{-\infty}^{\infty} d\omega \hat{f}(k, \omega) \hat{g}^*(k, \omega) \hat{\psi}^*(ac^{1/2}k, ac^{-1/2}\omega). \qquad (A3)$$

By making a change of variables a and c for fixed k and ω such that $k' = ac^{1/2}k$ and $\omega' = ac^{-1/2}\omega$, one finally obtains

$$I = C_\delta \langle f, g \rangle, \qquad (A4)$$

where

$$C_\delta = 2\pi \int_0^{\infty} \frac{dk}{|k|} \int_0^{\infty} \frac{d\omega}{|\omega|} \hat{\psi}^*(k, \omega) < \infty. \qquad (A5)$$

Considered as an operator on the signal f, one can see that the linear functionals $\int_0^{\infty} da/a^2 \int_0^{\infty} dc/c \int_{-\infty}^{\infty} db \int_{-\infty}^{\infty} d\tau W(b, \tau; a, c) \langle \delta_{b,\tau}, \_ \rangle$ and $C_\delta \langle f, \_ \rangle$ accomplish the same operation. With this in mind, one can obtain the

$$I_2 = (2\pi)^2 \int_0^{\infty} \frac{da}{a} \int_0^{\infty} \frac{dc}{c} \int_{-\infty}^{\infty} db \int_{-\infty}^{\infty} d\tau \left| \hat{f}(k, \omega) \right|^2 \left| \hat{\psi}^*(ac^{1/2}k, ac^{-1/2}\omega) \right|^2. \qquad (B2)$$

With the same change of variables as used in appendix A, one can finally obtain $I_2 = C_\psi \langle f, f \rangle$, where

$$C_\psi = (2\pi)^2 \int_0^{\infty} \frac{dk}{|k|} \int_0^{\infty} \frac{d\omega}{|\omega|} \left| \hat{\psi}^*(k, \omega) \right|^2. \qquad (B3)$$

APPENDIX C

Wavelet Scales and Fourier Wavelengths

Here we consider the relationship between wavelet scales and Fourier wavelengths so that we can relate results obtained from wavelet analysis to the Fourier framework that has been widely used. The consideration made here is quite similar to Meyers et al. (1993) except for $(1 + 1) - D$. As with Meyers et al. (1993), we consider the wavelet of a plane wave $f(x, t) = e^{i(kx + \omega t)}$. Then the STWT becomes

$$W(b, \tau; a, c) = 2\pi a \hat{\psi}^*(ac^{1/2}k, ac^{-1/2}\omega) e^{i(k_1 b + \omega_1 \tau)}. \qquad (C1)$$

Thus, the wavelet power spectrum becomes

$$\langle \delta_{b,\tau}, g \rangle = \frac{1}{2\pi} \int_{-\infty}^{\infty} dk \int_{-\infty}^{\infty} d\omega \hat{g}^*(k, \omega) e^{-i(kb + \omega\tau)}. \qquad (A2)$$

Thus, with the aid of (3) one can obtain

reconstruction equation (4) in the end. It is now also clear why the admissibility condition is necessary.

APPENDIX B

Proof of Energy Conservation

Similar to appendix A, consider the following integration:

$$I_2 = \int_0^{\infty} \frac{da}{a^3} \int_0^{\infty} \frac{dc}{c} \int_{-\infty}^{\infty} db \int_{-\infty}^{\infty} d\tau |W(b, \tau; a, c)|. \qquad (B1)$$

With the aid of (3), one obtains

$$|W(a, c)|^2 = (2\pi a)^2 \left| \hat{\psi}^*(ac^{1/2}k, ac^{-1/2}\omega) \right|^2. \qquad (C2)$$

Using (12),

$$|W(a, c)|^2 = (2\pi a)^2 \exp[-(ac^{1/2}k - k_0')^2 - (ac^{-1/2}\omega - \omega_0')^2], \qquad (C3)$$

so $\partial |W(a, c)|^2 / \partial a = 0$ and $\partial |W(a, c)|^2 / \partial c = 0$ give pairs of (a, c) in which the wavelet power spectrum has a local maximum. Ignoring unrealistic solutions, one gets the following relationship:

$$a_M = \frac{1}{2} \sqrt{\frac{k_M' \omega_M'}{k\omega}} > 0 \qquad (C4)$$

and

$$c_M = \frac{k_M'}{k} \frac{\omega}{\omega_M'} > 0 \qquad (C5)$$

in which $k_M' = (k_0' + \sqrt{k_0'^2 + 2}) \operatorname{sgn} k_0'$ and $\omega_M' = \omega_0' + \sqrt{\omega_0'^2 + 2}$. Note that wavelength is $2\pi/k$ and period is $2\pi/l$.

REFERENCES

Addison, P. S., 2002: *The Illustrated Wavelet Transform Handbook.* Taylor & Francis, 400 pp.

Antoine, J. P., R. Murenzi, P. Vandergheynst, and S. T. Ali, 2004: *Two-Dimensional Wavelets and Their Relatives.* Cambridge University Press, 458 pp.

Bessafi, M., and M. C. Wheeler, 2006: Modulation of south Indian Ocean tropical cyclones by the Madden–Julian oscillation and convectively coupled equatorial waves. *Mon. Wea. Rev.,* **134,** 638–656.

Bouyoucef, K., and R. Murenzi, 1995: Spatio-temporal wavelet transform: Application to target detection and recognition. *Automatic Object Recognition V,* F. A. Sadjadi, Ed., International Society for Optical Engineering (SPIE Proceedings, Vol. 2485), 32–43, doi:10.1117/12.213098.

Chen, T. C., and J. M. Chen, 1993: The 10–20-day mode of the 1979 Indian monsoon: Its relation with the time variation of monsoon rainfall. *Mon. Wea. Rev.,* **121,** 2465–2482.

Daubechies, I., 1992: *Ten Lectures on Wavelets.* Society for Industrial and Applied Mathematics, 357 pp.

Ding, Q. H., and B. Wang, 2007: Intraseasonal teleconnection between the summer Eurasian wave train and the Indian monsoon. *J. Climate,* **20,** 3751–3767.

Farge, M., 1992: Wavelet transforms and their applications to turbulence. *Annu. Rev. Fluid Mech.,* **24,** 395–457.

Fournier, A., 2000: Introduction to orthonormal wavelet analysis with shift invariance: Application to observed atmospheric blocking spatial structure. *J. Atmos. Sci.,* **57,** 3856–3880.

Frank, W. M., and P. E. Roundy, 2006: The role of tropical waves in tropical cyclogenesis. *Mon. Wea. Rev.,* **134,** 2397–2417.

Ge, Z., 2007: Significance tests for the wavelet power and the wavelet power spectrum. *Ann. Geophys.,* **25,** 2259–2269.

Haertel, P. T., G. N. Kiladis, A. Denno, and T. M. Rickenbach, 2008: Vertical-mode decompositions of 2-day waves and the Madden–Julian oscillation. *J. Atmos. Sci.,* **65,** 813–833.

Hayashi, Y., 1982: Space–time spectral analysis and its applications to atmospheric waves. *J. Meteor. Soc. Japan,* **60,** 156–171.

Hendon, H. H., and B. Liebmann, 1994: Organization of convection within the Madden–Julian oscillation. *J. Geophys. Res.,* **99,** 8073–8083.

——, and M. L. Salby, 1994: The life cycle of the Madden–Julian oscillation. *J. Atmos. Sci.,* **51,** 2225–2237.

Houze, R. A., 2004: Mesoscale convective systems. *Rev. Geophys.,* **42,** RG4003, doi:10.1029/2004RG000150.

Johnson, R. H., T. M. Rickenbach, S. A. Rutledge, P. E. Ciesielski, and W. H. Schubert, 1999: Trimodal characteristics of tropical convection. *J. Climate,* **12,** 2397–2418.

Kawamura, R., T. Murakami, and B. Wang, 1996: Tropical and mid-latitude 45-day perturbations over the western Pacific during the northern summer. *J. Meteor. Soc. Japan,* **74,** 867–890.

Kikuchi, K., and Y. N. Takayabu, 2004: The development of organized convection associated with the MJO during TOGA COARE IOP: Trimodal characteristics. *Geophys. Res. Lett.,* **31,** L10101, doi:10.1029/2004GL019601.

——, and B. Wang, 2008: Diurnal precipitation regimes in the global tropics. *J. Climate,* **21,** 2680–2696.

Kiladis, G. N., and M. Wheeler, 1995: Horizontal and vertical structure of observed tropospheric equatorial Rossby waves. *J. Geophys. Res.,* **100,** 22 981–22 997.

——, K. H. Straub, and P. T. Haertel, 2005: Zonal and vertical structure of the Madden–Julian oscillation. *J. Atmos. Sci.,* **62,** 2790–2809.

——, M. Wheeler, P. T. Haertel, K. H. Straub, and P. E. Roundy, 2009: Convectively coupled equatorial waves. *Rev. Geophys.,* **47,** RG2003, doi:10.1029/2008RG000266.

Kumar, P., and E. Foufoula-Georgiou, 1997: Wavelet analysis for geophysical applications. *Rev. Geophys.,* **35,** 385–412.

Lau, K.-M., and L. Peng, 1987: Origin of low-frequency (intraseasonal) oscillations in the tropical atmosphere. Part I: Basic theory. *J. Atmos. Sci.,* **44,** 950–972.

——, and H. Weng, 1995: Climate signal detection using wavelet transform: How to make a time series sing. *Bull. Amer. Meteor. Soc.,* **76,** 2391–2402.

Madden, R. A., and P. R. Julian, 1971: Detection of a 40–50 day oscillation in the zonal wind in the tropical Pacific. *J. Atmos. Sci.,* **28,** 702–708.

——, and ——, 1972: Description of global-scale circulation cells in tropics with a 40–50 day period. *J. Atmos. Sci.,* **29,** 1109–1123.

Majda, A. J., and J. A. Biello, 2004: A multiscale model for tropical intraseasonal oscillations. *Proc. Natl. Acad. Sci. USA,* **101,** 4736–4741.

——, S. N. Stechmann, and B. Khouider, 2007: Madden–Julian Oscillation analog and intraseasonal variability in a multicloud model above the equator. *Proc. Natl. Acad. Sci. USA,* **104,** 9919–9924.

Maloney, E. D., and D. L. Hartmann, 1998: Frictional moisture convergence in a composite life cycle of the Madden–Julian oscillation. *J. Climate,* **11,** 2387–2403.

Matsuno, T., 1966: Quasi-geostrophic motions in the equatorial area. *J. Meteor. Soc. Japan,* **44,** 25–43.

Matthews, A. J., and G. N. Kiladis, 1999: The tropical–extratropical interaction between high-frequency transients and the Madden–Julian oscillation. *Mon. Wea. Rev.,* **127,** 661–677.

Meyers, S. D., B. G. Kelly, and J. J. O'Brien, 1993: An introduction to wavelet analysis in oceanography and meteorology: With application to the dispersion of Yanai waves. *Mon. Wea. Rev.,* **121,** 2858–2866.

Miura, H., M. Satoh, T. Nasuno, A. T. Noda, and K. Oouchi, 2007: A Madden–Julian oscillation event realistically simulated by a global cloud-resolving model. *Science,* **318,** 1763–1765.

Moncrieff, M. W., M. Shapiro, J. Slingo, and F. Molteni, 2007: Collaborative research at the intersection of weather and climate. *WMO Bull.,* **56,** 206–211.

Morlet, J., G. Arens, E. Fourgeau, and D. Giard, 1982a: Wave propagation and sampling theory—Part I: Complex signal and scattering in multilayered media. *Geophysics,* **47,** 203–221.

——, ——, ——, and ——, 1982b: Wave propagation and sampling theory—Part II: Sampling theory and complex waves. *Geophysics,* **47,** 222–236.

Nakazawa, T., 1988: Tropical super clusters within intraseasonal variations over the western Pacific. *J. Meteor. Soc. Japan,* **66,** 823–839.

Nitta, T., 1987: Convective activities in the tropical western Pacific and their impact on the Northern Hemisphere summer circulation. *J. Meteor. Soc. Japan,* **65,** 373–390.

Pires, P., J.-L. Redelsperger, and J.-P. Lafore, 1997: Equatorial atmospheric waves and their association to convection. *Mon. Wea. Rev.,* **125,** 1167–1184.

Reed, R. J., and E. E. Recker, 1971: Structure and properties of synoptic-scale wave disturbances in the equatorial western Pacific. *J. Atmos. Sci.,* **28,** 1117–1133.

Roundy, P. E., 2008: Analysis of convectively coupled Kelvin waves in the Indian Ocean MJO. *J. Atmos. Sci.,* **65,** 1342–1359.

Rui, H., and B. Wang, 1990: Development characteristics and dynamic structure of tropical intraseasonal convection anomalies. *J. Atmos. Sci.,* **47,** 357–379.

Seiki, A., and Y. N. Takayabu, 2007: Westerly wind bursts and their relationship with intraseasonal variations and ENSO. Part I: Statistics. *Mon. Wea. Rev.,* **135,** 3325–3345.

Sikka, D. R., and S. Gadgil, 1980: On the maximum cloud zone and the ITCZ over Indian longitudes during the southwest monsoon. *Mon. Wea. Rev.,* **108,** 1840–1853.

Strang, G., and T. Nguyen, 1996: *Wavelets and Filter Banks.* 2nd ed. Wellesley-Cambridge Press, 520 pp.

Straub, K. H., and G. N. Kiladis, 2002: Observations of a convectively coupled Kelvin wave in the eastern Pacific ITCZ. *J. Atmos. Sci.,* **59,** 30–53.

——, and ——, 2003a: Interactions between the boreal summer intraseasonal oscillation and higher-frequency tropical wave activity. *Mon. Wea. Rev.,* **131,** 945–960.

——, and ——, 2003b: The observed structure of convectively coupled Kelvin waves: Comparison with simple models of coupled wave instability. *J. Atmos. Sci.,* **60,** 1655–1668.

Takayabu, Y. N., 1994: Large-scale cloud disturbances associated with equatorial waves. Part I: Spectral features of the cloud disturbances. *J. Meteor. Soc. Japan,* **72,** 433–449.

——, and M. Murakami, 1991: The structure of super cloud clusters observed in 1–20 June 1986 and their relationship to easterly waves. *J. Meteor. Soc. Japan,* **69,** 105–125.

——, and T. Nitta, 1993: 3–5-day-period disturbances coupled with convection over the tropical Pacific Ocean. *J. Meteor. Soc. Japan,* **71,** 221–246.

——, K. M. Lau, and C. H. Sui, 1996: Observation of a quasi-2-day wave during TOGA COARE. *Mon. Wea. Rev.,* **124,** 1892–1913.

Torrence, C., and G. P. Compo, 1998: A practical guide to wavelet analysis. *Bull. Amer. Meteor. Soc.,* **79,** 61–78.

Wang, B., 1988: Dynamics of tropical low-frequency waves: An analysis of the moist Kelvin wave. *J. Atmos. Sci.,* **45,** 2051–2065.

——, 2005: Theory. *Intraseasonal Variability in the Atmosphere-Ocean Climate System,* W. K.-M. Lau and D. E. Waliser, Eds., Praxis, 307–360.

——, and H. Rui, 1990: Dynamics of the coupled moist Kelvin–Rossby wave on an equatorial beta plane. *J. Atmos. Sci.,* **47,** 397–413.

——, and Y. Wang, 1996: Temporal structure of the Southern Oscillation as revealed by waveform and wavelet analysis. *J. Climate,* **9,** 1586–1598.

——, and X. Xie, 1996: Low-frequency equatorial waves in vertically sheared zonal flow. Part I: Stable waves. *J. Atmos. Sci.,* **53,** 449–467.

——, and ——, 1997: A model for the boreal summer intraseasonal oscillation. *J. Atmos. Sci.,* **54,** 72–86.

——, and X. Zhou, 2008: Climate variation and prediction of rapid intensification in tropical cyclones in the western North Pacific. *Meteor. Atmos. Phys.,* **99,** 1–16.

Weng, H., and K.-M. Lau, 1994: Wavelets, period-doubling, and time–frequency localization with application to organization of convection over the tropical western Pacific. *J. Atmos. Sci.,* **51,** 2523–2541.

Wheeler, M., and G. N. Kiladis, 1999: Convectively coupled equatorial waves: Analysis of clouds and temperature in the wavenumber–frequency domain. *J. Atmos. Sci.,* **56,** 374–399.

——, ——, and P. J. Webster, 2000: Large-scale dynamical fields associated with convectively coupled equatorial waves. *J. Atmos. Sci.,* **57,** 613–640.

Yasunari, T., 1979: Cloudiness fluctuations associated with the Northern Hemisphere summer monsoon. *J. Meteor. Soc. Japan,* **57,** 227–242.